Journal of Molecular Catalysis A: Chemical 308 (2009) 174–181

Contents lists available at ScienceDirect

Journal of Molecular Catalysis A: Chemical

journal homepage: www.elsevier.com/locate/molcata

Photocatalytic activity of V^{5+}, Mo^{6+} and Th^{4+} doped polycrystalline TiO_2 for the degradation of chlorpyrifos under UV/solar light

L. Gomathi Devi*, B. Narasimha Murthy, S. Girish Kumar

Department of Post Graduate Studies in Chemistry, Central College City Campus, Dr. Ambedkar Street, Bangalore University, Bangalore 560001, Karnataka, India

ARTICLE INFO

Article history:
Received 5 December 2008
Received in revised form 8 April 2009
Accepted 16 April 2009
Available online 23 April 2009

Keywords:
Chlorpyrifos
Transition metal ion doping
Th^{4+} ion doping
UV–vis spectroscopy
Solar light illumination

ABSTRACT

TiO_2 photocatalysts were prepared by doping transition metal ions like V^{5+}, $Mo^{6+}$and an inner transition metal Th^{4+} in the concentration range of 0.02–0.1% and were characterized by various analytical techniques. The photocatalytic activities of these catalysts were studied for the mineralization of chlorpyrifos (CP) as a probe molecule. X-ray diffraction results showed only anatase phase irrespective of nature, oxidation state and concentration of these dopants. The photocatalytic activity of undoped TiO_2 showed a better activity under UV light compared to doped catalysts. Under solar light illumination, the Th^{4+} (0.06%)–TiO_2 showed highest activity for the mineralization of CP. This was attributed to the prolonged separation of photogenerated electron–hole pairs, high specific surface area of the catalyst and high concentration of surface adsorbed water/hydroxyl groups. Further large shift in the absorption band (460 and 482 nm) due to the creation of mid band gap states by Th^{4+} dopant and also by its small crystallite size additionally contributes to the enhancement of the degradation process. The degradation pathway was followed by UV–vis spectroscopic and GC–MS analysis.

1. Introduction

Photocatalysis based on TiO_2 semiconductor is very promising and it has attracted extensive interest for the mineralization of pollutants both in air [1,2] and water [3–5]. Titania based photocatalysis has advantages such as strong resistance to chemicals, resistance to photo corrosion, ambient operational temperature and its low cost have led the relevant applications to the stage of commercialization. The current bottleneck with photocatalysis lies in its low quantum yield which is due to the competition between rates of surface charge carrier transfer to the rate of electron–hole recombination. Further, TiO_2 can only utilize relatively small part of the solar spectrum (<5%) for photocatalytic oxidation due to its wide band gap. The improvement in photocatalytic activity of TiO_2 is one of the most important aspects of heterogeneous photocatalysis. Attempts have been made to overcome the above problems by doping the TiO_2 matrix with various transition metal ions [6–11]. Doping within certain limits serves to prolong the lifetime of charge carriers if the dopants have energy levels just below the conduction band or just above the valence band which acts as charge carrier trapping centers and also results in the extension of their wavelength response towards the visible region. Further doping with lanthanides has shown to stabilize anatase phase and increases the adsorption capacities of organic pollutants at the semiconductor surface. This is due to the interaction of f orbital of lanthanide ions with the functional group of organic pollutants which attributes for its increased photoactivity [12–17]. Metal ions with vacant d and f orbital are expected to behave as Lewis acid. The chlorpyrifos (CP) which is a Lewis base forms a strong complex on the catalyst surface. The complex formation tendency increases in the presence of vacant f-orbital. Doping with various lanthanide ions (La^{3+}, Ce^{3+}, Er^{3+}, Pr^{3+}, Gd^{3+}, Nd^{3+}, Sm^{3+}, Yb^{3+}, Eu^{2+}, Nb^{5+}) has been extensively reported [12,13,18]. To our knowledge doping of a metal ion with 5f electronic configuration into the TiO_2 matrix is hardly known.

In view of this, the present research work mainly focuses on the process of doping of V^{5+} (3d series), Mo^{6+} (4d series) and Th^{4+} (5f series) into the TiO_2 matrix. The photocatalytic activities of these catalysts were investigated for the degradation of CP under both UV and solar illumination.

CP is one of the world's most widely used organophosphorus pesticides in agriculture. Exposure to CP and its metabolites has been related to a variety of nerve disorders in humans. Chlorpyrifos shows a wide spectrum of biological activity and is used to control range and forage insect pests as well as soil dwelling grubs, rootworms, borers and subterranean termites. The contamination has been found up to about 24 km from the site of application. Symptoms of acute poisoning include headache, nausea, muscle twitching and convulsions and in some extreme cases even death. Human birth defects have also been associated with exposure to CP and its products. It also affects the male reproductive system. CP is toxic to a variety of beneficial arthropods including bees, ladybird

* Corresponding author. Tel.: +91 80 22961336; fax: +91 80 22961331.
E-mail address: gomatidevi_naik@yahoo.co.in (L.G. Devi).

1381-1169/$ – see front matter © 2009 Elsevier B.V. All rights reserved.
doi:10.1016/j.molcata.2009.04.007

beetles and parasitic wasps. It kills fish at concentrations as low as a few parts per trillion [19].

2. Experimental

2.1. Chemicals

Titanium tetrachloride [$TiCl_4$], ammonium vanadate [NH_4VO_3] and ammonium molybdate [$(NH_4)_6Mo_7O_{24}{\cdot}4H_2O$] were supplied from Merck Chemicals. Thorium nitrate [$Th(NO_3)_4$], was obtained from Sisco-Chem Industries, Bombay. CP was obtained from Rallies Research Limited. The structure of the pesticide is shown in Fig. 1.

2.1.1. Catalyst preparation

Anatase form of TiO_2 nanoparticles were prepared by sol–gel method [20]. 25 ml of diluted $TiCl_4$ was taken along with 1 ml of concentrated H_2SO_4 and diluted to 1 l using double distilled water. Liquor NH_3 was added to the solution so as to maintain the solution pH in the range of 7–8. The precipitate is filtered and washed free of chloride and ammonium ions. The precipitate is first oven dried at 100 °C for 12 h and grinded in a mortar for about 1 h. The obtained powder is then calcined at 550 °C for 4.5 h to get pure anatase TiO_2.

Thorium nitrate [$Th(NO_3)_4$], ammonium vanadate [NH_4VO_3] and ammonium molybdate [$(NH_4)_6Mo_7O_{24}{\cdot}4H_2O$] were used as the source for Th^{4+}, V^{5+} and Mo^{6+} ions. Calculated amount of anatase TiO_2 along with the known volume of metal ion solution in the concentration ranges of 0.02%, 0.06% and 0.1% is taken. This mixture was grinded in mortar for 1 h and oven dried at 100 °C. The oven dried powder was calcined at 550 °C for 4.5 h.

2.1.2. Analytical instruments

The crystallite phase of the sample and variation of lattice parameter upon doping with metal ions were determined by X-ray diffraction (XRD) measurements using Philips powder diffractometer PW/1050/70/76 with Cu Kα radiation. The specific surface area of the powders was measured by dynamic Brunauer Emmett Teller (BET) method in which N_2 gas was adsorbed at 77 K using Digisorb 2006 surface area, pore volume analyzer Nova Quanta Chrome corporation instrument multipoint BET adsorption system. FTIR spectra were recorded using Nicollet IMPACT 400 D FTIR spectrometer, over the range of frequencies from 4000 to 400 cm^{-1} using KBr as the reference sample. The diffuse reflectance spectra (DRS) of the photocatalyst sample in the wavelength range of 200–800 nm were obtained by UV–vis scanning spectrophotometer (31031 PC UV-VIS-NIR instrument) using $BaSO_4$ as reference standard. The band gaps of photocatalysts were calculated by using the Kubelka–Munk method. Surface morphology was analyzed by SEM analysis using JSM 840 microscope operating at 25 kV on specimen upon which a thin layer of gold had been evaporated and an electron microprobe was used in the EDX mode to obtain quantitative information of the metal ions incorporated into the TiO_2 lattice.

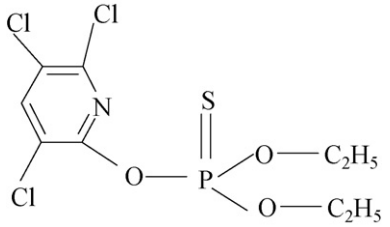

Fig. 1. Structure of CP.

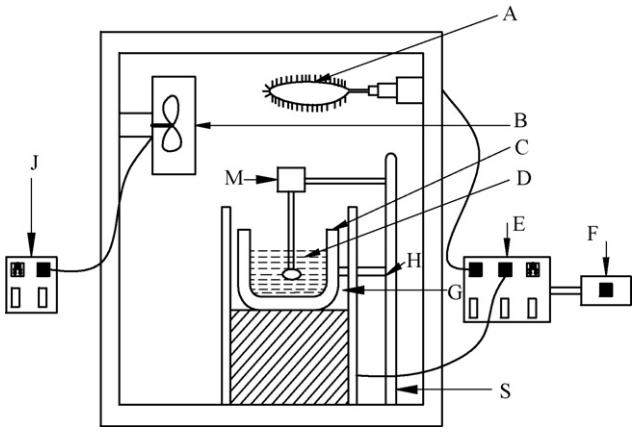

Fig. 2. Schematic diagram of reactor configuration: A, mercury vapor lamp [125 W]; B, fan; C, pyrex glass reactor; D, experimental solution; E, stabilizer; F, switch box; G, thermostat; H, clamp; J, switch box; M, motor; S, stand.

2.1.3. Photochemical reactor

UV light source used is a 125 W medium pressure mercury vapor lamp and the photon flux is found to be 7.75 mW/cm^2 as determined by ferrioxalate actinometry. The wavelength emission is around 350–400 nm. The photoreactor is a circular glass vessel with surface area of 176 cm^2. The light was made to focus directly into reaction mixture at a distance of 29 cm in the presence of atmospheric oxygen as shown in Fig. 2. Experiments using solar light were carried out between 11 am and 2 pm during the summer season in Bangalore, India. At this interval the fluctuation in solar intensity was minimal. The latitudes and longitudes are 12.58°N and 77.38°E respectively. The average intensity of the sunlight is found to be around 1200 W m^{-2}. The intensity of solar light was concentrated using a convex lens and the reaction mixture was exposed to this concentrated solar light. The initial pH of the solution was 5.51 and final pH is 5.89.

2.1.4. Degradation procedure

At desired time intervals the samples were collected and centrifuged to separate the photocatalysts and were subjected to UV–vis spectroscopic analysis using Shimadzu UV-1700 pharmaspec UV-visible spectrophotometer. These samples were extracted into non-aqueous ether medium and were subjected to GC–MS analysis using GC-MS-QP 5000 Shimadzu mass spectrometer to identify the photoproducts during the course of the reaction.

3. Results and discussion

3.1. Structural characterization of photocatalysts

3.1.1. XRD analysis

XRD results showed that irrespective of the nature of the dopants, their concentration and its oxidation states, all the doped samples showed only anatase phase. The average crystallite size was calculated in accordance with Scherer's equation:

$$D = \frac{k\lambda}{\beta \cos\theta} \quad (1)$$

where k is the constant (shape factor, about 0.9), λ is the X-ray wavelength (0.15418 nm), β is the full width at half maximum (FWHM) of the diffraction line and θ is the diffraction angle. The values of β and θ are taken for crystal plane (1 0 1) of anatase phase. In the present case Th^{4+} doping effectively hinders the growth of crystallite size and hence suppresses the anatase to rutile phase transformation. Due to the absence of rutile phase in the doped TiO_2 samples, it can be proposed that all the dopants can act as substitutional impu-

Table 1
Lattice parameter, unit cell volume and crystallite size from XRD analysis for all the photocatalysts.

Photocatalyst	2θ of crystal plane (1 0 1) of anatase	Lattice parameters (Å)	Unit cell volume (Å^3)	Crystallite size (nm)
TiO_2 (0.00%)	25.32	3.7828 ± 0.0003; 9.5023 ± 0.0005	135.97	26.34
Th–TiO_2 (0.02%)	25.35	3.7822 ± 0.0006; 9.5123 ± 0.0013	136.07	24.28
Th–TiO_2 (0.06%)	25.38	3.7826 ± 0.0008; 9.5293 ± 0.0004	136.34	24.29
Th–TiO_2 (0.10%)	25.36	3.7814 ± 0.0006; 9.5301 ± 0.0012	136.27	30.28
V–TiO_2 (0.02%)	25.34	3.7822 ± 0.0004; 9.5113 ± 0.0007	136.05	26.24
V–TiO_2 (0.06%)	25.36	3.7824 ± 0.0009; 9.5136 ± 0.0005	136.10	26.30
V–TiO_2 (0.10%)	25.33	3.7825 ± 0.0006; 9.5152 ± 0.0007	136.13	28.42
Mo–TiO_2 (0.02%)	25.34	3.7801 ± 0.0009; 9.5209 ± 0.0005	136.04	26.28
Mo–TiO_2 (0.06%)	25.36	3.7801 ± 0.0008; 9.5406 ± 0.0002	136.32	26.40
Mo–TiO_2 (0.10%)	25.33	3.7809 ± 0.0003; 9.5212 ± 0.0004	136.10	29.38

rity. Burns et al. reported that Nd^{3+} ion occupies lattice positions of Ti at lower dopant concentration and interstitial site at higher dopant concentration (>0.1%) [21]. In this line of reasoning, the concentration of Th did not exceed 0.1%. Thus it can be proposed that Th^{4+} has occupied lattice positions of Ti in TiO_2. Since the dopant concentration is low, its incorporation into the TiO_2 lattice creates oxygen vacancies which are still insufficient to facilitate rutile phase transformation. Therefore nucleation of rutile phase is prevented resulting in the enhanced stability of anatase phase. Due to similarity in the ionic size of Mo^{6+} (0.062 nm) and V^{5+} (0.059 nm) with that of Ti^{4+} (0.068 nm) it can be easily substituted into the TiO_2 lattice at Ti lattice position which is further confirmed by the Vegards's law (change in the unit cell dimension should be linear with change in the composition) confirming the possibility of metal ion as a substituent in TiO_2 lattice [22,23]. It can be observed from Table 1 that unit cell parameter along *c*-axis increases with dopant concentration up to 0.06% linearly. It is reported that in the case of metal oxides there is critical value of dispersion capacity, at values lower than which the oxide might become highly dispersed on the support without the formation of a separate crystalline phase [24]. Since, no characteristic peaks corresponding to Th, V and Mo species is present, it can be concluded that the metal ion loading is below the dispersion capacity.

The diffraction peaks of crystal planes (1 0 1), (2 0 0) and (2 0 4) in anatase phase are selected to determine lattice parameters of doped samples. On doping with metal cations (Th^{4+}, V^{5+} and Mo^{6+}), diffraction angle of the crystal plane (1 0 1) of anatase phase shows a slight shift to the higher angles which confirms the incorporation of metal cations into TiO_2 matrix. This shift is higher for Th^{4+} dopant compared to V^{5+} and Mo^{6+} dopants (both shows almost similar shifts). This can be attributed to ionic size of Th^{4+} which is larger than Ti^{4+}. This is also confirmed by the calculation of lattice parameters which shows the higher elongation of *c*-axis for Th^{4+}–TiO_2 samples compared to other V^{5+}–TiO_2 and Mo^{6+}–TiO_2 samples. Due to the similarity in ionic radii of V^{5+} and Mo^{6+} with that of Ti^{4+}, similar variation in lattice parameter along *c*-axis were observed for both the samples. The variation in lattice parameter and also increase in the unit cell volume of doped samples compared to undoped TiO_2 confirms the fact that the dopant has entered the TiO_2 matrix. However, for higher dopant concentration (0.1%) slight decrease in the diffraction angle of the crystal plane (1 0 1) of anatase was observed for all the dopants.

3.1.2. UV–vis and diffuse reflectance spectral studies

All the doped photocatalysts showed a clear red shift attributed to the creation of mid band gap states and this can also be due to decrease in their crystallite size as shown in Fig. 3. The extent of shift depends on the nature and concentration of the metal ion. For all the dopants, increase in the red shift was observed when the dopant concentration was increased from 0.02% to 0.06%. Beyond this dopant concentration, absorption band shows a slight blue shift. The similar trend was observed for the variation in the crystallite size and surface area. The band gaps calculated from the Kubleka–Monk plot are shown in Table 2. The band gap is governed by factors like crystallite size and the defects in the TiO_2 network. Sanchez and Lopez [25] suggested that lowering of band gaps was caused by stoichiometric deficiency of Ti/O ratios. When TiO_2 is doped with transition metals like V^{5+} and Mo^{6+} ions n-type behavior is expected. Therefore 3d and 4d orbitals of the dopants (V^{5+} and Mo^{6+}) create mid band gap states just below the conduction band. Red shifts for these metal doped catalysts are attributed to the charge transfer transition between the 'd' orbitals of the dopants and band gap states of TiO_2. The color of V^{5+}–TiO_2 catalyst was comparable to that of TiO_2, while Mo^{6+}–TiO_2 catalyst shows light brown color with a red shift of 480 nm (450 nm for V^{5+}–TiO_2 catalyst). Though the charges on Th and Ti are same, the incorporation of Th^{4+} in TiO_2 lattice is always accompanied by creation of oxygen vacancies due to its higher ionic size. These oxygen vacancies may be doubly ionized/singly ionized/neutral. Two absorption edges at 466 and 486 nm were observed in the visible region for Th^{4+}–TiO_2 catalysts. The band at 480 nm may be due to the presence of Ti^{3+} in TiO_2 lattice. The absorption edge at 460 nm may arise from the charge transfer transition between the 'd' and 'f' orbitals of the dopants to the band gap states of TiO_2.

3.1.3. Induced defect states by the dopants in the pristine TiO_2

Considering the ionic size and the oxidation states of the dopants the following defect states can be proposed in accordance with Krogner–Vink notation [22,26]:

Table 2
UV–vis absorption λ_{max} and the band gap from diffuse reflectance spectra using Kubelka–Munk plot.

Photocatalyst	λ_{max} (nm)	Mid band gap states, E_g (eV)
TiO_2	390	3.1
Th^{4+} (0.02%)–TiO_2	436	2.8
Th^{4+} (0.06%)–TiO_2	460 and 482	2.6 and 2.5
Th^{4+} (0.1%)–TiO_2	410	3.0
V^{5+} (0.02%)–TiO_2	424	2.9
V^{5+} (0.06%)–TiO_2	456	2.6
V^{5+} (0.1%)–TiO_2	446	2.7
Mo^{6+} (0.02%)–TiO_2	420	2.9
Mo^{6+} (0.06%)–TiO_2	480	2.5
Mo^{6+} (0.1%)–TiO_2	446	2.7

- *Case 1*: if the incorporation of dopants creates conduction band electrons, then:

$$V_2O_5 \leftrightarrow 2V_{Ti}^{\bullet} + 2e^- + 4Oo + \frac{1}{2}O_2 \quad (2)$$

$$Mo_2O_6 \leftrightarrow 2Mo_{Ti}^{\bullet\bullet} + 4Oo + 4e^- + O_2 \quad (3)$$

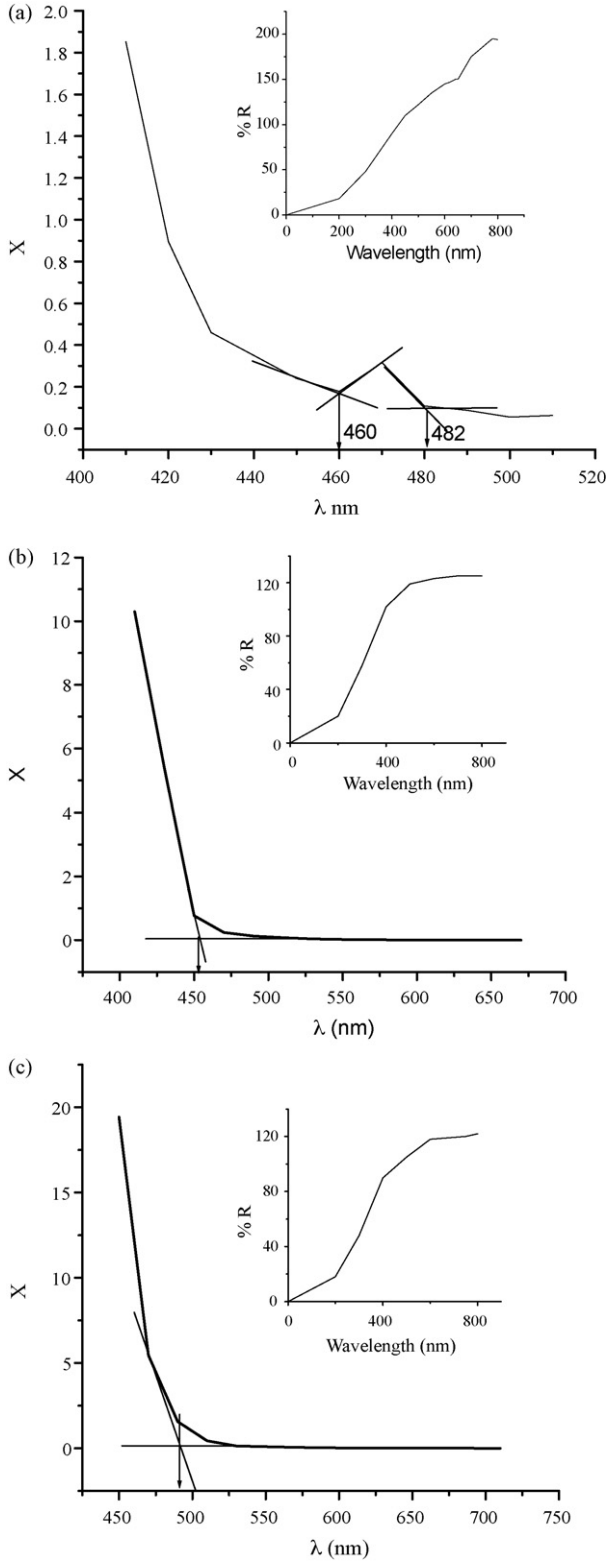

Fig. 3. Kubelka–Munk plot of X versus wavelength where $X=(1-R_\infty)^2/2R_\infty$. The inset in the figure refers to the diffused reflectance spectra (DRS) of the respective catalyst. (a) Th^{4+} (0.06%)–TiO_2; (b) V^{5+} (0.06%)–TiO_2; (c) Mo^{6+} (0.06%)–TiO_2.

- *Case 2*: instead of creating conduction electrons, charge compensation can also be achieved by defects such as interstitial oxygens:

$$V_2O_5 \leftrightarrow 2Vi_{Ti}^{\bullet} + O_i'' + 4Oo \quad (4)$$

$$Mo_2O_6 \leftrightarrow 2Moi_{Ti}^{\bullet\bullet} + O_i'' + 4Oo \quad (5)$$

- *Case 3*: if oxides are completely soluble then the dopants occupies substitution site creating oxygen vacancies:

$$V_2O_5 \leftrightarrow 2V_{Ti}^{\bullet} + Vo'' + 4Oo \quad (6)$$

$$Mo_2O_6 \leftrightarrow 2Mo_{Ti}^{\bullet\bullet} + 2Vo'' + 4Oo \quad (7)$$

$$ThO_2 \leftrightarrow Th_{Ti} + Vo^{\bullet\bullet} + Oo + (1/2)O_2 + e^-$$

$$(\text{since ionic radius of } Th^{4+} > Ti^{4+}) \quad (8)$$

The imbalance in the charge created on doping can also be compensated by titanium vacancies:

$$2V_2O_5 \leftrightarrow 4V_{Ti}^{\bullet} + V_{Ti}''' + 10Oo \quad (9)$$

$$2Mo_2O_5 \leftrightarrow 4Moi_{Ti}^{\bullet\bullet} + 2V_{Ti}''' + 12O_6 \quad (10)$$

The mechanisms involved are complex and it is difficult to predict the exact effect of dopants in TiO_2 matrix.

3.1.4. FT-IR analysis

FTIR spectra were recorded using KBr and anatase TiO_2/doped TiO_2 in the ratio 9:1. The spectra of undoped TiO_2 and M–TiO_2 (M = Th^{4+}, V^{5+} and Mo^{6+}) show a broad band near 3426 cm^{-1} and at 1654 cm^{-1}. The surface adsorbed water shows bands around 3400 and 1630 cm^{-1} while surface adsorbed hydroxyl groups (Ti-OH) are expected to show bands around 3563, 3172 and 1600 cm^{-1} [27–30]. Therefore the peaks near 3426 and 1654 cm^{-1} were attributed to surface adsorbed water and hydroxyl groups. The peak at 3426 cm^{-1} was broadened for the sample Th^{4+} (0.06%)–TiO_2 compared to all the other samples which may be due to their smaller crystallite size. It is observed that doped samples have higher concentration of surface adsorbed water than undoped TiO_2 may be due to the increase in surface area. However the samples with higher dopant concentration M–TiO_2 (~0.1%), showed a lesser capacity to adsorb water and hydroxyl groups due to decrease in the surface area of the samples. The highest concentration of these groups on the Th^{4+} (0.06%)–TiO_2 was attributed to largest surface area compared to all the other samples. When cation having positive charge higher than 4+ is substituted in TiO_2 lattice, an imbalance in the positive charge is created which attracts hydroxide anion on to the photocatalyst surface. Since the charge on molybdenum is 6+ it may attract two hydroxyl groups on to the surface while vanadium being in 5+ can attract only one hydroxyl group [31]. But in the case of Th which is in 4+ oxidation state, the hopping mechanism observed in Ti (Ti^{3+}/Ti^{4+}) and its smaller crystallite size is mainly responsible for the adsorption of these groups. The photogenerated electrons can get trapped on the surface of TiO_2 which may result in the formation of Ti^{3+} centers. This concentration of Ti^{3+} increases with surface area. For photocatalytic reactions, surface adsorbed water and hydroxyl groups are crucial. The concentration of adsorbed water and hydroxyl groups on the photocatalyst surface is directly related to the surface acid base properties of the sample.

3.1.5. Specific surface area measurements, scanning electron microscopy (SEM) observations and energy dispersive X-ray (EDX) analysis

The specific surface area of the undoped TiO_2 and M–TiO_2 (M = Th^{4+}, V^{5+} and Mo^{6+}) are reported in Table 3. All the doped samples had higher surface area compared to undoped TiO_2 confirming

Table 3
Specific surface areas of various photocatalysts and their adsorption capacities in the dark.

Photocatalyst	BET specific surface area (m^2/g)	% of pesticide adsorbed
TiO_2	18	8.5
Th^{4+} (0.02%)–TiO_2	26	17.5
Th^{4+} (0.06%)–TiO_2	34	20.5
Th^{4+} (0.1%)–TiO_2	32	19.2
V^{5+} (0.02%)–TiO_2	23	14.2
V^{5+} (0.06%)–TiO_2	26	17.9
V^{5+} (0.1%)–TiO_2	24	11.0
Mo^{6+} (0.02%)–TiO_2	25	16.0
Mo^{6+} (0.06%)–TiO_2	28	18.5
Mo^{6+} (0.1%)–TiO_2	22	13.5

the substitution of the dopants in TiO_2 lattice. Th^{4+} (0.06%)–TiO_2 samples had the highest surface area due to its smallest crystallite size compared to all the other photocatalysts. SEM revealed similar morphology and homogeneous distribution of all the dopants while EDX analysis confirmed the metal ion incorporation into the TiO_2 matrix.

3.2. Photocatalytic degradation of chlorpyrifos

3.2.1. Adsorption studies

The pesticide solution was stirred along with photocatalysts (150 mg) in dark for 10 min. The amount of adsorption was calculated by comparing the concentration of pesticide before and after stirring. The saturation amount of pesticide adsorbed on the different photocatalysts before the irradiation is shown in Table 3. The percentage of pesticide adsorption was calculated from $(1 - C/C_0) \times 100$, where C_0 and C are initial concentration and residual concentration of pesticide respectively. The adsorption experiments showed that Th^{4+} (0.06%)–TiO_2 has the highest adsorption capacity, while V^{5+} (0.1%)–TiO_2 had the least. The decreasing adsorption capacity of the catalysts is of the order: Th^{4+} (0.06%)–TiO_2 > Th^{4+} (0.1%)–TiO_2 > Mo^{6+} (0.06%)–TiO_2 > V^{5+} (0.06%)–TiO_2 > Th^{4+} (0.02%)–TiO_2 > Mo^{6+} (0.02%)–TiO_2 > V^{5+} (0.02%)–TiO_2 > Mo^{6+} (0.1%)–TiO_2 > V^{5+} (0.1%)–TiO_2 > TiO_2. All the doped samples showed stronger adsorption capacities than undoped TiO_2.

3.2.2. Photocatalytic activity under UV light/sunlight

Degradation was negligible in the absence of catalyst when the solution was irradiated with UV/solar light for the period of 2.5 h. Hence it was confirmed that decrease in the concentration of pesticide in the presence of either UV light or solar light was originated from the photocatalytic effect of TiO_2 and doped TiO_2. Undoped TiO_2 shows the highest rate constant compared to all the doped TiO_2 samples under UV light. This may be due to the fact that mid band gaps created by the dopants may serve as site for recombination. The degradation reaction follows first-order kinetics indicated by the linearity of the plot $-\log C/C_0$ versus time. Within the doped samples, Mo^{6+}–TiO_2 (0.06%) showed highest activity while V^{5+}–TiO_2 (0.1%) showed least activity under UV light. Their respective rate constants are shown in Fig. 4 and Table 4. Under solar irradiation, only 13% of the pesticide was degraded after 2.5 h of irradiation with undoped TiO_2 due to its wide band gap. Among the doped samples, Th^{4+}–TiO_2 (0.06%) showed enhanced activity compared to all the other doped samples. This is due to the large red shift in the band gap (482 nm) which makes it sensitive to absorb more number of photons under solar light. The decrease in the reactivity of the doped catalyst under solar light is of the order: Th^{4+} (0.06%)–TiO_2 > Th^{4+} (0.1%)–TiO_2 ≈ Mo^{6+} TiO_2 (0.06%) > Th^{4+} (0.02%)–TiO_2 > Mo^{6+} (0.1%)–TiO_2 > Mo^{6+} (0.02%)–TiO_2 > V^{5+} (0.06%)–TiO_2 > V^{5+} (0.02%)–TiO_2 > V^{5+} (0.1%)–TiO_2. The highest activity for Th^{4+} (0.06%)–TiO_2 can be attributed to its (i) large surface area, (ii) large shift in the band gap, (iii) higher concentration of surface adsorbed water and hydroxyl groups, and (iv) doping Th^{4+} into TiO_2 matrix (0.06%) might result in effective separation of electrons and holes.

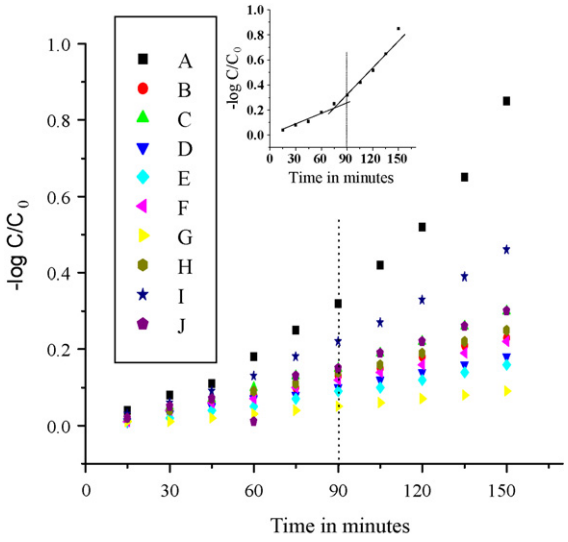

Fig. 4. Plot of $-\log C/C_0$ versus time for the degradation of pesticide using M–TiO_2 where M = Th^{4+}/V^{5+}/Mo^{6+} catalysts under UV light: (A) TiO_2, (B) Th^{4+} (0.02%)–TiO_2, (C) Th^{4+} (0.06%)–TiO_2, (D) Th^{4+} (0.0%)–TiO_2, (E) V^{5+} (0.02%)–TiO_2, (F) V^{5+} (0.06%)–TiO_2, (G) V^{5+} (0.1%)–TiO_2, (H) Mo^{6+} (0.02%)–TiO_2, (I) Mo^{6+} (0.06%)–TiO_2, and (J) Mo^{6+} (0.1%)–TiO_2. The inset plot shows the two stage first-order kinetics between intervals 0–90 min and 90–150 min for the doped catalysts.

The optimum dopant concentration was found to be 0.06% for all the three dopants. This suggests that there exist an optimum dopant concentration for these metal cations in TiO_2 matrix which leads to efficient separation of photogenerated electron and hole pairs. At this optimum concentration of dopants, the surface barriers becomes higher and the space charge region extends leading to the efficient separation of electrons and holes within the space charge region, due to the electric field experienced by the charge carriers. For higher dopant concentration (0.1%) the space charge region becomes narrow and the penetration depth of light into TiO_2 greatly exceeds the space charge layer which increases the rate of recombination of electrons and holes. These results suggest that there exists a optimal dopant concentration and maximum width in the space charge region at which charged carriers can be separated effectively. Based on the experimental results obtained, we have proposed that the defect levels created by Th^{4+} ions in the TiO_2 lattice can capture the photogenerated electrons or holes shallowly and detrap the same to adsorbed oxygen and hydroxyl ions respectively to generate super oxide radicals and hydroxyl radicals. These processes not only suppress the recombination rate but also generate the excess free radicals necessary for the degradation reaction. For the other doped catalysts, detrapping of the charge carriers becomes difficult as they are deeply trapped which decreases the catalytic activity.

3.2.3. Determination of rate constant

The first-order rate constant 'k' was calculated from the plot of $-\log C/C_0$ versus time (Figs. 4 and 5). The curves show two different linear stages which indicate that the photocatalytic degradation follows first-order kinetics in two stages [32,33]. The rate constant for the second stage is twice than that of first stage for TiO_2 as shown in Table 4. In the first stage, it is proposed that the hydroxyl radicals attacks the side chain of the chlorpyrifos molecule which has less electron density compared to the aromatic ring. The reaction

Table 4
Calculation of first-order rate constants in two stages of the reaction: (i) 0–90 min and 90–150 min for UV light photocatalysis; (ii) 0–60 min and 75–150 min for solar light photocatalysis.

Photocatalyst	Rate constant, k ($\times 10^{-2}$ min^{-1})			
	UV light photocatalysis		Visible light photocatalysis	
	Ist stage	IInd stage	Ist stage	IInd stage
TiO_2	3.1	6.3	0.38	–
Th^{4+} (0.02%)–TiO_2	1.48	–	2.0	3.6
Th^{4+} (0.06%)–TiO_2	1.82	–	3.5	7.1
Th^{4+} (0.1%)–TiO_2	1.19	–	2.3	4.0
V^{5+} (0.02%)–TiO_2	1.04	–	0.6	0.6
V^{5+} (0.06%)–TiO_2	1.38	–	1.5	1.6
V^{5+} (0.1%)–TiO_2	0.59	–	1.0	1.1
Mo^{6+} (0.02%)–TiO_2	1.61	–	1.6	2.3
Mo^{6+} (0.06%)–TiO_2	2.2	3.6	2.6	6.0
Mo^{6+} (0.1%)–TiO_2	1.7	1.7	2.6	3.5

rate involving this side chain with hydroxyl radical is slow [34]. Therefore the rate constant for this reaction is less compared to the second stage. While in the second stage, the hydroxyl radicals might attack of electron rich aromatic ring whose degradation kinetics proceeds at a faster rate and hence shows a higher rate constant. While for Mo^{6+}–TiO_2 (0.06%) the rate constant for the second stage is 1.6 times higher than first stage and for Mo^{6+} (0.1%)–TiO_2 the rate constant for the second stage is 1.5 times higher than the first stage. For other photocatalysts, reaction followed first-order kinetics for the entire span of the experiment under UV light. The catalyst Th^{4+}–TiO_2 (0.06%) shows highest rate constant under solar light which may be due to the efficient separation of charged carriers. Similar values of rate constants were obtained for V^{5+}–TiO_2 catalyst both in the first and the second stage.

3.2.4. UV spectroscopic analysis

CP is characterized by the absorption bands at 210, 235 and 295 nm in the UV region. The band at 210 nm corresponds to the 'E' band which arises due to the electronic transition in the pyridinyl ring. The bands at 235 and 295 nm may be attributed to the susbtituents on the pyridine ring. On UV irradiation with the TiO_2 photocatalyst, the band at 295 nm slightly reduces its intensity and shows a blue shift to 284 nm and a new band appears at 223 nm. Formation of chloro (–Cl) substituted pyridine derivative gives rise to the band at 284 nm and the band at 223 nm may be attributed to hydroxyl (–OH) substituted pyridine derivative. This confirms that the degradation proceeds in the initial stage by the loss of side chain attached to the pyridine ring. The band at 284 nm shows further blue shift to 260 nm which may be due to the formation of pyridine [35] while the band at 223 nm reduces its intensity on irradiating the reaction solution up to 90 min. These observations show that the substituents chloro (–Cl) and (–OH) groups may be eliminated as HCl and H_2O. After 2 h of illumination no characteristic bands appeared in the UV region which confirms the complete cleavage of chromophores in the CP molecule. Complete degradation was not achieved for the doped catalysts under UV illumination even after 3 h. This suggests that TiO_2 is the better photocatalyst for the degradation of organic contaminants under UV light. Under solar light only 10% of the pesticide was degraded with TiO_2 (in 2 h) while complete degradation of the pesticide was achieved with in 45 min for Th^{4+} (0.06%)–TiO_2 samples (as further supported by GC–MS analysis).

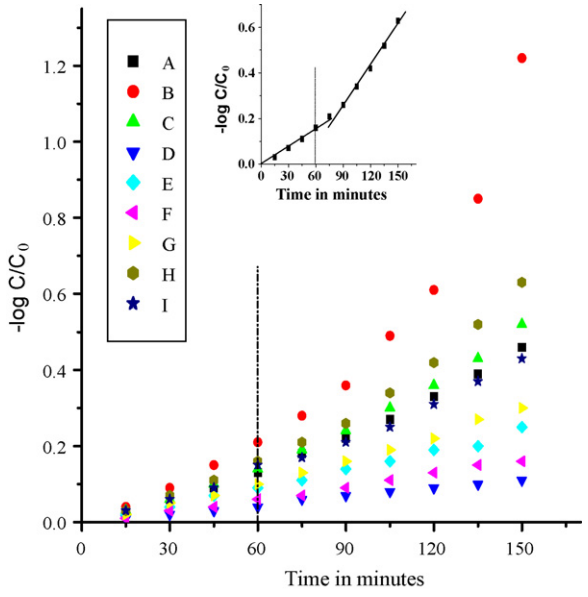

Fig. 5. Plot of $-\log C/C_0$ versus time for the degradation of pesticide using M–TiO_2 where M = Th^{4+}/V^{5+}/Mo^{6+} catalysts under solar light: (A) Th^{4+} (0.02%)–TiO_2, (B) Th^{4+} (0.06%)–TiO_2, (C) Th^{4+} (0.0%)–TiO_2, (D) V^{5+} (0.02%)–TiO_2, (E) V^{5+} (0.06%)–TiO_2, (F) V^{5+} (0.1%)–TiO_2, (G) Mo^{6+} (0.02%)–TiO_2, (H) Mo^{6+} (0.06%)–TiO_2, and (I) Mo^{6+} (0.1%)–TiO_2. The inset plot shows the two stage first-order kinetics between intervals 0–60 min and 90–150 min for the doped catalysts.

3.2.5. GC–MS analysis

The photocatalytic degradation of CP yielded a number of transient organic intermediates. The CP solution showed intense m/z peak at 351 before irradiation. The sample after 30 min of UV irradiation showed one m/z peak at 335. This intermediate **(1)** formation is due to the result of hydroxyl radicals attack at the –P=S bond converting to –P=O (oxon derivative) which is a primary characteristic product formed during the photocatalytic oxidation of organo phosphorous compound [36,37]. This indicates that the degradation proceeds through the loss of sulfur atom as sulfate group. After 60 min of UV irradiation, the sample showed m/z peak at 199 attributed to 2-hydroxy 3,5,6 tri-chloro pyridine **(2)**, 138 **(3)** and 154 **(4)** of medium intensity due to the formation of substituted alkyl phosphates. The two possible proposed pathways are

(i) Hydroxyl radicals may attack the intermediate **(1)** at the site of –P=O group leading the formation of OH–P=O derivative **(3)** and intermediate **(2)**.
(ii) Hydrogen radicals might attack at the site of –P=O group leading the formation of H–P=O derivative **(4)** and intermediate **(2)**.

It is interesting to note that intermediate **(2)** is formed in both the cases which is the most stable intermediate in the present study. After 90 min of irradiation the observed m/z peaks at 95, 130, 165 and 183 are due to the formation of 2-hydoxy pyridine **(5)**, 6-chloro,2-hydroxy pyridine **(6)**, 3,5 dichloro-2-hydroxy pyridine

(7) and 2,3,5 tri-chloro pyridine **(8)**. The possible ways of formation of various intermediates starting from **(2)** may be explained as follows:

(i) Intermediate **(2)** may react with three hydrogen radicals eliminating all the three chloro (–Cl) groups as HCl leading to the formation of intermediate **(5)**.
(ii) The chloro group at the positions of 2 and 5 in the intermediate **(2)** might react with two hydrogen radicals resulting in the formation of **(6)**.
(iii) The chloro group at the position 4 might react with one hydrogen radical leading to the formation of **(7)**.
(iv) The –OH group at the position 2 in the intermediate **(2)** might be eliminated as water molecule resulting in **(8)**. However the involvement of hydroxyl radicals in the above reactions cannot be ruled out. Though the hydroxyl can substitute –Cl, it can be easily eliminated as water molecule resulting in the same intermediates. The GC–MS spectra recorded for 105 min showed *m*/*z* peak at 79 due to the formation of pyridine **(9)**. The chloro group (–Cl) and the hydroxyl group (–OH) in the intermediates **(5)**, **(6)**, **(7)** and **(8)** might be lost as HCl and H_2O molecules giving **(9)**. After 120 min of irradiation the subsequent reaction of hydroxyl radicals with **(9)** leads to mineralization of the pesticide. The *m*/*z* peaks of the intermediates **(3)** and **(4)** persisted till 90 min and phosphorous present in the compound may be eliminated as phosphates. The higher number of compounds detected during the degradation of the above compound shows the complexity in the degradation mechanism and suggests the existence of various degradation routes resulting in complex and interconnected pathways.

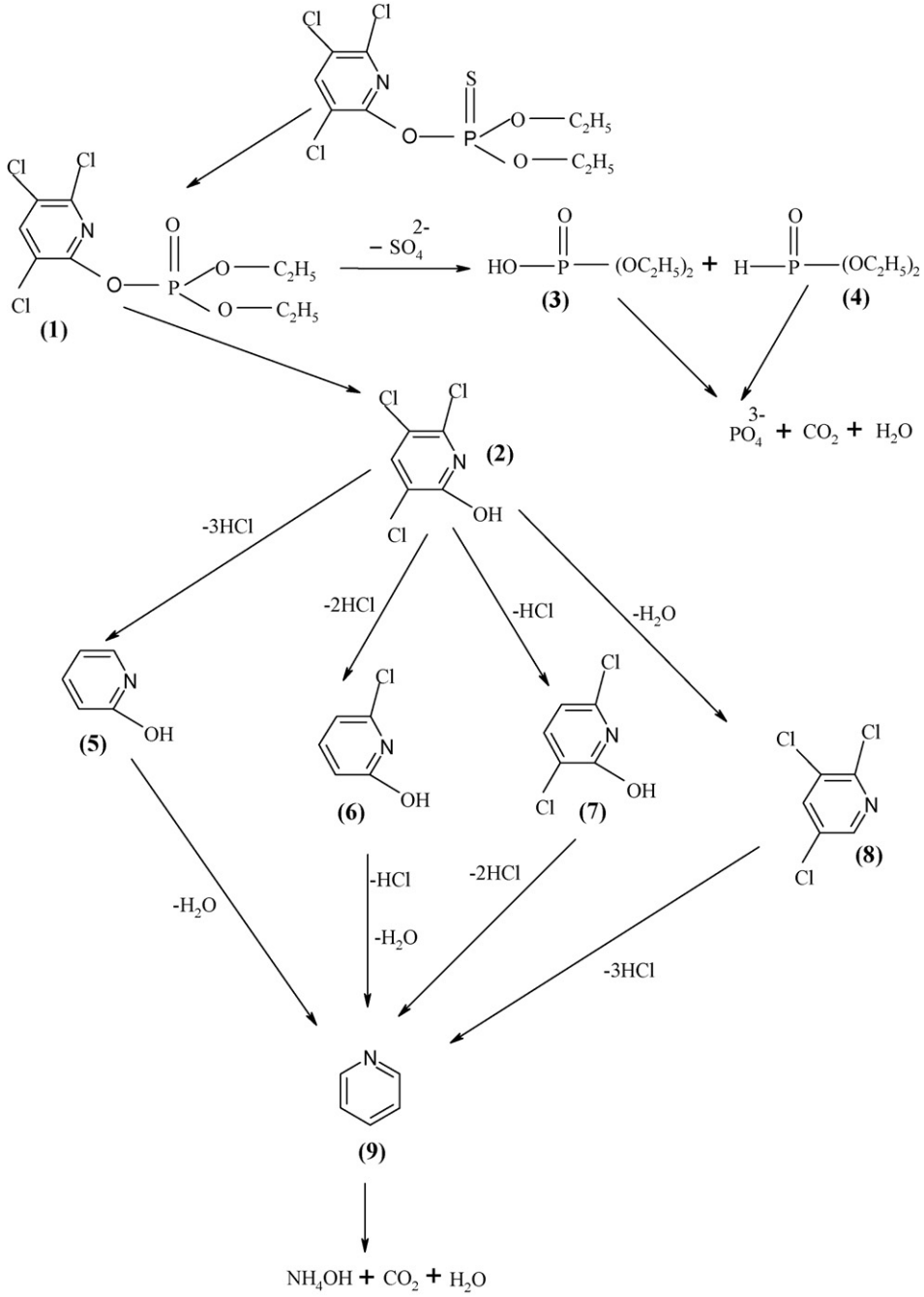

Scheme 1. Photodegradation pathway for CP.

When the chlorpyrifos was irradiated with sunlight using Th^{4+} (0.06%)–TiO_2, intermediates **(2)**, **(3)** and **(5)** were the major product and **(9)** was the minor product. This was attributed to enhancement in process due to the generation of excess free radicals under solar light which has destroyed the intermediates at faster rate. Hence it can be concluded that the use of solar energy is advantageous as it enhances the photocatalytic process and avoids the complexity in the degradation mechanism owing to the formation of less number of intermediates. The degradation pathways are shown in Scheme 1.

4. Conclusion

TiO_2 doped with Th^{4+}, V^{5+} and Mo^{6+} and their activity was studied on the degradation of chlorpyrifos as the probe reaction. Anatase phase was confirmed for all the doped photocatalysts by XRD analysis. Th^{4+} (0.06%)–TiO_2 showed enhanced activity compared to all the other catalysts under solar light due to the high surface area of the sample and also due to the higher capacity to surface adsorb water and hydroxyl groups. The larger shift in the absorption band (460 and 482 nm) to visible region increases the efficiency of the photocatalysts to absorb more photons under solar light. The degradation was followed by UV–vis spectroscopy and GC–MS analysis.

Acknowledgements

Financial assistance from UGC Major Research Project (2007–2010), Government of India is acknowledged. One of the authors B. Narasimha Murthy acknowledges to C.M.R. Institute of Technology for their support.

References

[1] N. Daneshvar, M.N. Rabani, M.A. Modirshahla, J. Photochem. Photobiol. A: Chem. 168 (2004) 39–45.
[2] L. Cermenati, P. Pichat, C. Guillard, A. Albini, J. Phys. Chem. B 101 (1997) 2650–2658.
[3] I. Bouzaida, C. Ferronato, J.M. Chovelon, M.E. Ramman, J.M. Herrmann, J. Photochem. Photobiol. A: Chem. 168 (2004) 23–30.
[4] K.P. Yu, G.W.M. Lee, Appl. Catal. B 75 (2007) 29–38.
[5] A. Nakajima, H. Obata, Y. Kameshima, K. Okada, Catal. Commun. 6 (2005) 716–720.
[6] L. Palmisano, A. Di Paola, G. Marci, M. Schiavello, K. Uosaki, S. Ikeda, B. Ohtani, J. Phys. Chem. B 106 (2002) 637–645.
[7] S.M. Chang, R.A. Doong, J. Phys. Chem. B 110 (2006) 20808–20814.
[8] Y. Segura, L. Chmielarz, P. Kustrowski, P. Cool, R. Dziembaj, E.F. Vansant, J. Phys. Chem. B 110 (2006) 948–955.
[9] B. Jongosomjit, T. Wongsalee, P. Praserthdam, Catal. Commun. 6 (2005) 705–710.
[10] K. Wilke, H.D. Breuer, J. Photochem. Photobiol. A: Chem. 12 (1999) 49–53.
[11] W. Choi, A. Termin, M.R. Hoffmann, J. Phys. Chem. 98 (1999) 13669–13679.
[12] K.T. Ranjit, I. Willner, S.H. Bossmann, A.M. Braun, Environ. Sci. Technol. 35 (2001) 1544–1549.
[13] A.W. Xu, Y. Gao, H.Q. Liu, J. Catal. 207 (2002) 151–157.
[14] F. Caimei, X. Peng, S. Yanping, J. Rare Earths 24 (2006) 309–313.
[15] K.V. Baiju, P. Periyat, W. Wunderlich, P.K. Pillai, P. Mukundan, K.G.K. Warrier, J. Sol–Gel. Sci. Technol. 43 (2007) 283–290.
[16] X.Z. Li, F.B. Li, C.H. Ao, S.C. Lee, M.F. Hou, Chemosphere 59 (2005) 787–800.
[17] J. Lin, J.C. Yu, J. Photochem. Photobiol. A: Chem. 116 (1998) 63–67.
[18] Z. Zhang, C.C. Wang, R. Zakaria, J.Y. Ying, J. Phys. Chem. B 102 (1998) 10871–10878.
[19] K.D. Racke, Rev. Environ. Contam. Toxicol. 131 (1993) 1–151.
[20] L.G. Devi, G.M. Krishnaiah, J. Photochem. Photobiol. A: Chem. 121 (1999) 141–145.
[21] A. Burns, G. Hayes, W. Li, J. Hirvonen, J.D. Demaree, S.I. Shah, Mater. Sci. Eng. B 111 (2004) 150–155.
[22] L.G. Devi, B.N. Murthy, Catal. Lett. 125 (2008) 320–330.
[23] V. Leonid, Azaroff, Introduction to Solids, Tata McGraw Hills, 2001.
[24] D.W. Bahnemann, J. Monig, R. Chapman, J. Phys. Chem. 91 (1987) 3782–3788.
[25] E. Sanchez, T. Lopez, Mater. Lett. 25 (1995) 271–275.
[26] F.A. Kroger, H.J. Vink, Solid State Physics, Academic Press, New York, 1956.
[27] Y. Suda, T. Morimoto, Langmuir 3 (1986) 786–790.
[28] K. Tanaka, J.M. White, J. Phys. Chem. 86 (1982) 4708–4714.
[29] Z. Ding, G.Q. Lu, P.F. Greenfield, J. Phys. Chem. B 104 (2000) 4815–4820.
[30] J. Yu, Y. Su, B. Cheng, M. Zhou, J. Mol. Catal. A 258 (2004) 104–112.
[31] J. Yu, J.C. Yu, W. Ho, Z. Jiang, L. Zhang, Chem. Mater. 14 (2002) 3808–3816.
[32] L.G. Devi, B.N. Murthy, S.G. Kumar, Catal. Lett., in press, doi:10.1017/s10562-009-9938-6.
[33] X.H. Wang, J.G. Li, H. Kamiyama, Y. Moriyoshi, T. Ishigaki, J. Phys. Chem. B 110 (2006) 6804–6809.
[34] I.K. Konstantinou, T.A. Albanis, Appl. Catal. B: Environ. 49 (2004) 1–14.
[35] M. Robert, G. Silverstein, Bassler Clayton, Terence C. Morrill, Spectrometric Identification of Organic Compounds, 4th edition, John Wiley and Sons, 1981.
[36] E. Evgenidou, I. Konstantinou, K. Fytianos, I. Poulios, T. Albanis, Catal. Today 124 (2007) 156–162.
[37] M. Kerzhentsev, Chantal Guillard, J.M. Herrmann, Pierre Pichat, Catal. Today 27 (1996) 215–220.